AUT Journal of Electrical Engineering
10.22060/EEJ.2025.24346.5688

Renewable Energy-Fed EV Charging Station Utilizing Z-Source Quadratic Improved Boost Zeta Converter with Optimized RBFNN MPPT Control

R. Sathish[1,*], V. Sekar[2]

[1]Research scholar, Department of Electrical and Electronics Engineering, School of Engineering and Technology, Dhanalakshmi Srinivasan University, Samayapuram, 621112, India.

[2]Dean, School of Engineering and Technology, Dhanalakshmi Srinivasan University, Samayapuram, 621112, India.

*Corresponding Author E-mail: rsathishme.13@gmail.com

Abstract:

PV-based EV charging stations offer economic advantages, including decreased operational costs, reduced grid dependency during peak hours, and enhanced consistency through the addition of local energy storage systems. This work presents a novel approach for integrating Renewable Energy Sources (RESs), specifically Photovoltaic (PV) systems, into Electric Vehicle (EV) charging stations. Proposed research utilizes a Z-source Quadratic Improved Boost Zeta (Z-SQ-IBZ) converter coupled with a Crayfish Optimization Algorithm based Radial Basis Function Neural Network (COA-RBFNN) Maximum Power Point Tracking (MPPT) algorithm for enhancing power extraction efficiency from PV arrays. Energy management and power balancing between PV energy generation and storage system are enabled through bidirectional DC-DC converter interfacing battery storage and DC link. Proposed PV-based EV charging system is implemented in MATLAB Simulink, and novel Z-SQ-IBZ converter attains enhanced efficiency of 96.63% with improved voltage and minimized voltage stress. The novel COA optimised RBFNN MPPT effectively tracks optimal power with improved tracking efficiency of 99.81%. MATLAB simulation results demonstrate that proposed topology effectively manages energy flow, optimises PV power utilisation, and constantly supports EV charging demands, making it appropriate for efficient EV charging station applications.

Keywords:

RES, PV, EV, Z-source Quadratic Improved Boost Zeta converter, COA-RBFNN MPPT algorithm.

1. Introduction

EV utilisation is rising exponentially worldwide, but the most crucial issue in EV adaptation is the shortage of charging infrastructure. As EV adoption rises, battery consumption also escalates [1]. Typically, EV batteries are replaced once their capacity falls below $70\% - 80\%$ of their original capacity, leading to a substantial number of retired batteries in a short time, which contributes to environmental pollution. To address this issue, a key solution lies in the echelon utilisation of the EV batteries. The growing carbon footprint from conventional grid-connected EV charging has prompted a global shift toward RES. In recent times, the importance of the RES has steadily grown in energy generation, replacing conventional energy sources with broader benefits across various applications. The transition to green energy signifies a new evolutionary phase for the energy sector, aiming for emission-free generation and utilisation [2-3]. The adoption of clean energy sources aims to mitigate environmental harm while enhancing the efficiency of charging systems. Solar energy, in particular, is increasingly recognised as a cost-effective solution for grid supplementation. Additionally, PV systems are highly advantageous due to their minimal maintenance needs in terms of labour and fuel. Moreover, PV-connected charging stations effectively address power demands on the utility grid [4-6].

PV produces low-voltage Direct Current (DC) power, which necessitates voltage boosting through DC converters. A wide range of power converter topologies is available. Boost, quadratic boost converter, Z-source network, Zeta converter, and boost-zeta [7]. By using an effective technique for DC-DC switching converter operations, a boost converter raises input voltage to a higher output voltage. However, it requires careful regulation to sustain stability, reduce losses, and accomplish desired efficiency levels, particularly under varying load and input conditions [8]. The quadratic boost converter offers a broad voltage conversion range, minimised electrical losses with reduced ripple. Despite their ability to achieve high gain, these converters face prominent drawbacks in pulsating source current [9]. Z-source network offers various advantages, including ability to increase/decrease voltage levels with reduced components and at a lower cost. Nevertheless, discontinuous input current limits the DC voltage utilisation with enhanced voltage stress [10]. The zeta converter boosts the voltage value of the input voltage given. It draws a line current that is directly proportional to the input voltage while avoiding the generation of harmonic currents. The restrictions on the duty cycle limit the range of voltage gain [11]. The boost-zeta converter utilises coupled inductors to achieve high voltage gain, reduced power switch stress, and lower costs, while its boost substructure effectively suppresses voltage spikes from leakage inductance. Nonetheless, requires a snubber circuit to recover leakage inductance energy and limit voltage spikes, adding complexity to the design [12].Consequently, this paper employs a Z-QIBZ converter to provide enhanced power for the EV charging applications. Figure 1 shows schematic illustration of proposed PV-based EV charging system.

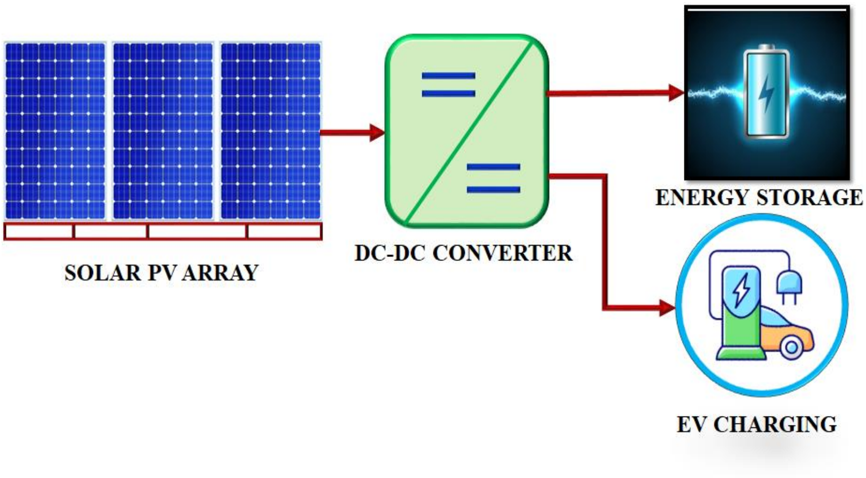

Fig. 1. Schematic representation of a proposed model

To capture peak power from solar panels, effective control algorithms need to be implemented. MPPT schemes are utilised to optimally track peak power from solar panels. In order to achieve maximum power, the process is made simpler by optimizing the duty cycle of the DC converter [13]. To do this, a number of techniques are available, such as Incremental Conductance (IC) and Perturb and Observe (P&O). The PV panel voltage is periodically increased or decreased using the P&O approach. The IC algorithm automatically adjusts the step size to optimise power output. In contrast, the fixed step size method cannot adapt in real-time, resulting in increased oscillations at the MPP. These conventional MPPT techniques often face limitations in accurately tracking the MPP of PV systems under rapidly fluctuating solar insolation. Additionally, these methods may cause ripples in output parameters like current $\left(I_{PV}\right)$, and voltage $\left(V_{PV}\right)$ [14-15]. Artificial Neural Network (ANN)-based MPPT ensures rapid response to climate changes, effectively captures MPP of PV panels while overcoming their nonlinear characteristics and adapting to weather fluctuations. Nonetheless, it gets trapped at a local maximum and struggles to track maximum power, resulting in reduced power generation [16]. Fuzzy-based MPPT controllers are widely used due to their adaptability to system uncertainties and nonlinear conditions, requiring no exact system model while efficiently tracking the maximum power point in dynamic environments. However, it experiences performance degradation during step-decreasing changes in environmental conditions due to overlapping membership function support values at low-duty ratio changes [17]. RBFNN-based MPPT controller is integrated for capturing optimal energy from PV system even under dynamic conditions. To further enhance performance of MPPT controller, advanced optimisation techniques are employed.

Table 1. Review of conventional MPPT optimised algorithms

Ref	Methodology	Contributions	Future Scope
18.	Genetic Optimised Algorithm (GAO)	Robust meta-heuristic method stimulated by biological processes, aimed at finding optimal solutions by quickly tracking MPP under varying atmospheric conditions.	Although the GAO offers benefits such as rapid convergence and minimal oscillation near the MPP, it has certain drawbacks. Specifically, this algorithm is not well-suited for extremely lengthy or complex problems.
19.	Grey Wolf Optimisation (GWO)	It imitates the group dynamics of grey wolves and offers an efficient solution for various optimisation problems with rapid convergence.	Efficacy of GWO is swayed by factors like selection of parameters, including the number of wolves and maximum iteration count.
20.	Particle Swarm Optimisation (PSO)	PSO techniques are employed to identify the MPP of PV arrays and regulate the energy storage components effectively.	PSO converges to local optima that fully explore the search space. It is ineffective in charging applications.
21	Whale Optimisation Algorithm (WOA)	WOA iteratively modifies duty cycle until MPP is reached, simulating hunting behaviour of humpback whales.	However, it causes disturbances in voltage and current of converter's work cycle.
22.	Ant Colony Optimisation (ACO)	ACO exhibits intelligent foraging behaviour of ant colonies that strategically adjust the duty cycle.	ACO loses its tracking ability during climatic changes and has a low convergence speed.
23.	Cuckoo Optimisation (CO)	It is inspired by the lifestyle of the cuckoo bird that effectively solves optimization problems.	Nonetheless, due to the transient oscillations, it influences the efficiency of the system.
24.	Multi-Objective Bayesian Optimization Algorithm (MOBOA)	MOBOA lessens power oscillations around MPP and strikes an efficient balance between exploration and exploitation.	Nevertheless, MOBOA produce large tracking errors.

The limitations are overcome by the proposed Novel COA that finely tunes the hyperparameters of the RBFNN MPPT controller by mimicking the bio-inspired behaviour of crayfish foraging activity. Thus, maximum power is extracted from the PV system for enhanced EV charging station applications.

1-1- Research Contribution

Solar PV systems contribute to addressing power shortages by offering a reliable electricity source for EV charging. This study enhances the real-world efficiency of solar PV charging stations. Additionally, it offers valuable guidance for developing solar PV charging infrastructure suitable for EVs, and various commercial applications within the region. Findings highlight a cost-effective, energy-efficient, and sustainable approach to utilising renewable energy, fostering the broader adoption of EVs. Additionally, the proposed system evaluates both the economic and environmental implications of solar energy. A comprehensive analysis is conducted to identify an optimal, low-emission, and budget-friendly model design.

The novelty of this manuscript is emphasised in the following steps:

- Power attained from PV system is improved with Z-SQ-IBZ converter, which produces enhanced power with relatively high voltage gain.
- Maximum power is extracted from PV system with an RBFNN MPPT controller, which rapidly adapts to the dynamic operational conditions.
- Performance of RBFNN MPPT controller is further enhanced by optimally tuning its hyperparameters by integration of COA
- Organisation of paper is as follows: Section 2 outlines methodology of current work. Section 3 details problem modelling process. Section 4 discusses outcomes of two distinct cases, and Section 5 provides concluding remarks for entire study.

2. Proposed Model Description

The escalating challenges of global warming and exhaustion of fossil fuels have amplified the importance of RES and EV in recent years. However, advancing these technologies necessitates the modernisation of the electric power infrastructure, which relies heavily on power electronic devices. Consequently, this research introduces an innovative Z-SQ-IBZ Converter, which is employed in this study to optimise low-voltage output of PV systems.

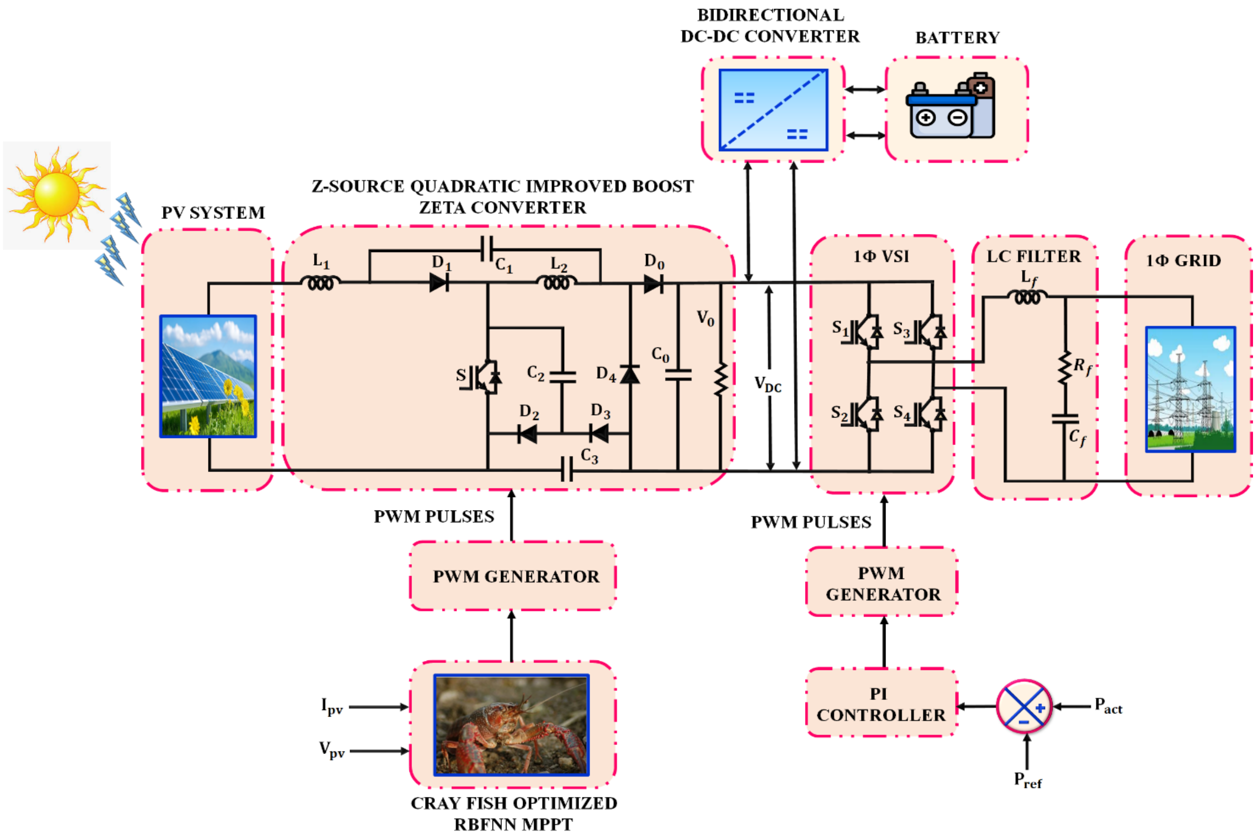

Fig. 2. Block diagram of proposed model

The proposed technique of delivering enhanced power for grid applications is given in Figure 2. A PV system produces electricity by converting solar energy into electrical energy. Output of PV system is boosted with hybrid Z-SQ-IBZ converter that provides enhanced power even under fluctuating conditions. To extract optimal power from solar panels, Crayfish optimised RBFNN-based MPPT is employed, which tracks MPP and generates control signals for the converter control operations. The control signal from the MPPT controller is fed to PWM generator that generates switching pulses for converter operations. DC power attained from converter is forwarded to a 1Φ VSI for DC to AC conversion. The inverter operations are controlled with a PI controller, which compares reference power and actual power, and adjusts the inverter operations effectively. Bidirectional converter regulates energy flow between the battery and the DC link, facilitating battery charging from either PV system or grid, and enabling power discharge to supply the grid. This system efficiently integrates solar power into the grid, leveraging advanced control techniques to optimise energy harvesting and ensure stability in power delivery.

3. Proposed System Modelling

3-1- PV Model

Solar PV module is built with connecting solar PV cells in series. It is a semiconductor device that generates electrical energy from solar radiation using photovoltaic process. When sunlight incident on panels, energy of photons exceeds the energy gap and generates an electric flow. Solar cell model is illustrated in the figure. 3

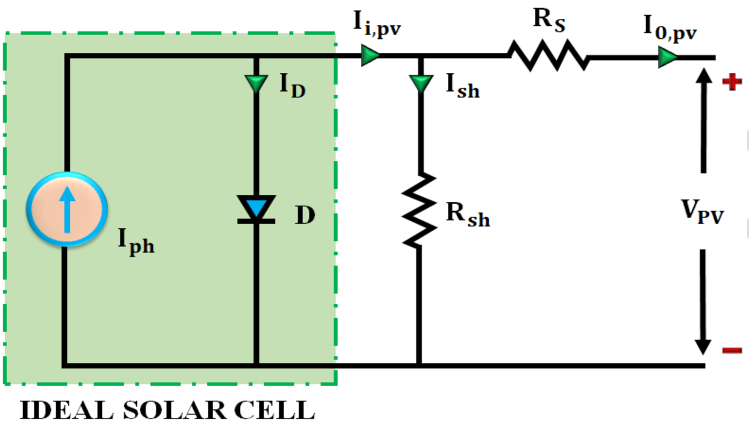

Fig. 3. Solar cell model

Output current, denoted as $\left(I_{0,PV}\right)$, of a PV cell is determined based on Kirchhoff's current law and is calculated using the corresponding equations.

$$\left(I_{0,PV}\right) = I_{ph} - I_D - I_{sh} \tag{1}$$

Where, photon offered current is I_{ph}, PV reverse saturation current is $I_D$and shunt current is I_{sh}. Eq. (2) mathematically represents the relationship between operating temperature and solar irradiation, the key factors responsible for generating current in the PV cell when it is activated by solar light.

$$I_{ph} = I_{SC} + \left[K_i \times \left(T_c - T_r\right) \times \left(\frac{G}{G_{STC}}\right)\right] \tag{2}$$

Under Standard Test Conditions (STC), short-circuit current of a PV cell is denoted by I_{SC}. Parameter K_i represents temperature coefficient associated with cells short-circuit current $\left(in\, A/K\right)$. Additionally, G refers to solar insolation incident on PV cell's surface area, expressed in $\left(W/sq.m.\right)$. T_r and T_c denote reference temperature and operating temperature of the cell, respectively. Similarly, I_0 stands for the reverse saturation current, which varies depending on environmental conditions and is mathematically calculated as shown in Eqn (3)

$$I_0 = \left(I_{0,STC}\right) \times \left\{ \left(\frac{T}{T_{STC}}\right)^3 \times e^{\left(\left(\frac{q.E_g}{k.A}\right).\left(\frac{1}{T} - \frac{1}{T_{STC}}\right)\right)} \right\} \tag{3}$$

Current flowing through diode is computed by Shockley equation,

$$I_D = I_0 \times \left(\left(e^{\frac{q.\left(V_{PV} + \left(I_{ph}.R_s\right)\right)}{V_T}} \right) - 1 \right) \tag{4}$$

Thermal voltage is V_T, and output voltage on load side of solar cells is V_{PV}. By using Ohm's law, current through shunt resistor is calculated,

$$I_{sh} = \frac{V_{PV} + \left(I_{ph}.R_s\right)}{R_{sh}} \tag{5}$$

The mathematical equation of single diode solar cell is as follows,

$$I_{o,PV} = I_{ph} - \left(I_0 \times \left(\left(e^{\frac{q.\left(V_{PV} + \left(I_{ph} R_s\right)\right)}{V_T}} \right) - 1 \right) - \frac{V_{PV} + \left(I_{ph}.R_s\right)}{R_{sh}} \right) \tag{6}$$

$$V_T = \frac{\left(N_{se} \times A \times k \times T\right)}{q} \tag{7}$$

Where, number of cells connected in series is N_{se}. Power attained from PV system is stepped up by DC converter. However, their optimised voltage and current characteristics of the PV system do not always align with the requirements of various electrical applications. Consequently, the development of enhanced power converters is essential to effectively transform and integrate energy generated by RES into practical usage.

3-2- Z-Source Quadratic Improved Boost Zeta Converter

A novel Z-SQ-IBZ converter is proposed in this study, it has a relatively modest duty cycle and a significant voltage gain. According to figure 4, proposed converter is made up of two inductors $\left(L_1\ and\ L_2\right)$ and three capacitors (C_1, C_2, C_3). Switch S and diodes D_2 and D_3 are used to control the capacitor C_2. Furthermore, capacitor C_3 is added to improve voltage boosting and increase gain. With the purpose of producing desired output voltage, basic idea is to store energy across all three capacitors and use them in series. By dividing the output voltage among several capacitors, voltage stresses are reduced and lower-rated parts in high-power system.

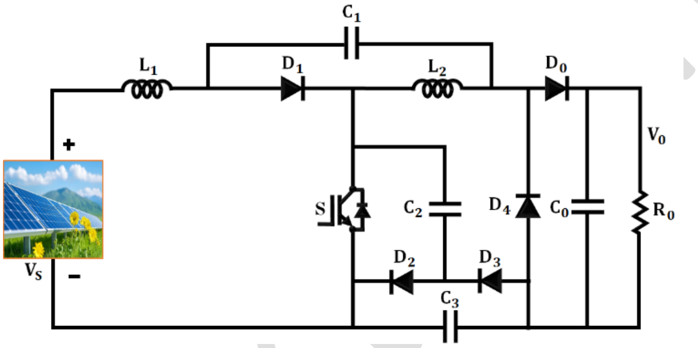

Fig. 4. Equivalent circuit of Z-SQ-IBZ converter

The proposed Z-SQ-IBZ converter operates in two different operating modes.

Mode 1: $\left(0 - \boldsymbol{DT_S}\right)$

As shown in figure.5, in this mode of operation, switch S is turned on, diodes D_1, D_2 and D_0 become reverse biased and stop conducting, while diodes D_3 and D_4 continue to conduct. During this phase, inductors L_1 and L_2, along with capacitor C_3, charge to their peak values, whereas capacitors C_1, C_2, and C_0 undergo discharge.

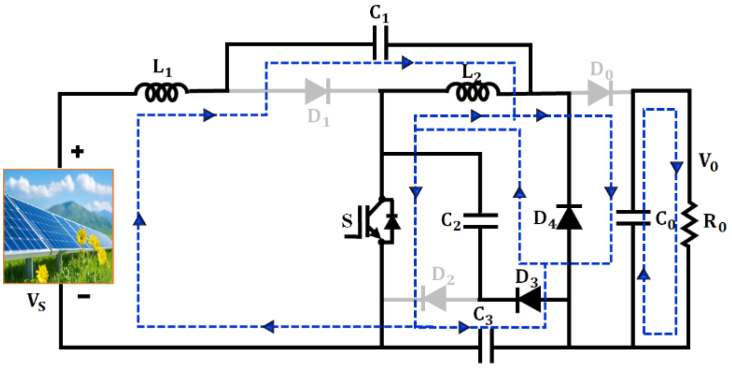

Fig. 5. Shoot through interval mode

The corresponding voltage and current expressions for the inductors and capacitors are well-defined as follows:

$$v_{L1} = v_S + v_{C1} + v_{C2} \quad (8)$$

$$v_{L2} = v_{C2} \quad (9)$$

$$i_{C1} = -i_{L1} \quad (10)$$

$$i_{C2} = -\left(i_{L1} + i_{L2} + i'_{C3}\right) \quad (11)$$

$$i_{C0} = -i_0 \quad (12)$$

The term i'_{C3} represents the average current passing through capacitor C_3 during this mode of operation.

Switching losses occur during the transition periods of the switch S.

$$P_{s,\,sw} = \frac{1}{2} V_s \cdot I_s \cdot \left(t_{on} + t_{off}\right) \cdot f_{sw} \quad (13)$$

Here, t_{on} and t_{off} are switching times and f_{sw} is switching frequency.

Mode 2: $\left(DT_S - T_s\right)$

Switch S is deactivated in this mode of operation, and circuit is shown in figure. 6. Diodes D_1, D_2 and D_0 become forward biased and start conducting as a result, while diodes D_3 and D_4 become reverse biased and cease conducting. Capacitors C_1, C_2, and C_0 charge throughout this time, while inductors L_1 and L_2 and capacitor C_3 discharge.

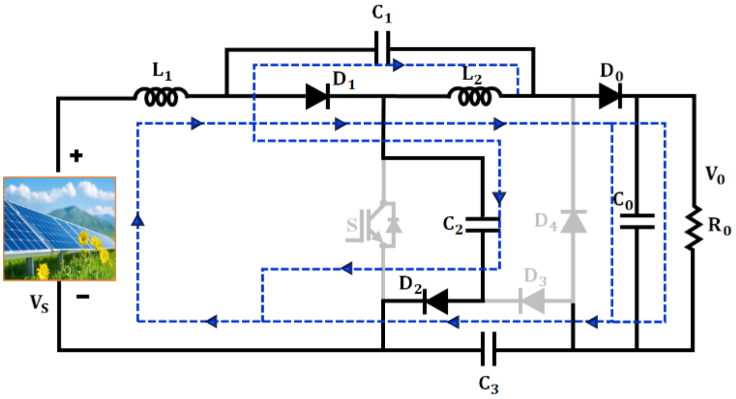

Fig. 6. Non-shoot through interval mode

The voltage expressions for the inductors and the current expressions for the capacitors are formulated as follows:

$$\mathrm{v_{L1} = v_S - v_{C2} = v_S + v_{C1} + v_{C3} - v_0} \tag{14}$$

$$\mathrm{v_{L2} = -v_{C1} = v_{C2} + v_{C3} - v_0} \tag{15}$$

$$\mathrm{i_{C1} = i_{L2} - i_0 - i'_{C0}} \tag{16}$$

$$\mathrm{i_{C2} = -i_{L1} - i_0 - i'_{C0}} \tag{17}$$

$$\mathrm{i_{C3} = -(i_0 + i'_{C0})} \tag{18}$$

Term i'_{C0} represents average current that flows through capacitor C_0 during this interval.

In steady-state operation of proposed converter, average current of capacitors and average voltage across inductors over one complete switching interval must equate to zero. Relationships are found by applying the volt-second balance principle to inductors L_1 and L_2 over the course of a full switching cycle.

$$V_{C1} = \frac{V_S D}{1+3D+D^2} \tag{19}$$

$$V_{C2} = V_{C3} = \frac{V_S * (1-D)}{1+3D+D^2} \tag{20}$$

$$V_0 = \frac{V_S (2-D)}{1+3D+D^2} \tag{21}$$

Under optimal conditions, input power matches output power, resulting in formulation of input current relationship.

$$V_S I_{L1} = V_0 I_0 \tag{22}$$

$$I_{L1} = \frac{(2-D)}{1+3D+D^2} I_0 \tag{23}$$

$$I'_{C0} = \frac{D}{1-D} I_0 \tag{24}$$

$$I'_{C3} = \frac{1}{D} I_0 \tag{25}$$

$$I_{L2} = \frac{1}{1+3D+D^2} I_0 \tag{26}$$

The boost factor is determined as follows:

$$B = \frac{V_0}{V_S} = \frac{2-D}{1+3D+D^2} \tag{27}$$

It is crucial to control inductor current ripples and capacitor voltage ripples within predetermined bounds in order to guarantee that the converter runs in Continuous Conduction Mode (CCM) and generate a positive, increased output voltage. Hence, V_0 and V_S retain the same polarity in practical operation, and the negative gain region is avoided in design. Appropriate sizing of passive components plays a significant role in achieving this. Following formulas for determining size of different components are derived from main equations regulating shoot-through and non-shoot-through intervals.

$$L_1 = \frac{\left(2+3D+D^2\right) V_S D}{\left(1+3D+D^2\right) f_{sw} \Delta i_{L1} \% * I_{L1}} \tag{28}$$

$$L_2 = \frac{(1-D) V_S D}{\left(1+3D+D^2\right) f_{sw} \Delta i_{L2} \% * I_{L2}} \tag{29}$$

$$C_1 = \frac{(2-D) I_0 D}{\left(1+3D+D^2\right) f_{sw} \Delta v_{C1} \% * V_{C1}} \tag{30}$$

$$C_2 = \frac{I_0}{\left(1+3D+D^2\right) f_{sw} \Delta v_{C2} \% * V_{C2}} \tag{31}$$

$$C_3 = \frac{I_0}{f_{sw}\Delta v_{C3}\%*V_{C3}} \tag{32}$$

$$C_0 = \frac{I_0 D}{f_{sw}\Delta v_{C0}\%*V_{C0}} \tag{33}$$

Current ripple percentage of inductor L_x and percentage of voltage ripple in the capacitor C_x are shown by symbols Δi_{Lx} and Δv_{Cx}, respectively. Selection of active components depends on voltage and current stresses they endure. Voltage stress levels experienced by diodes are outlined as follows:

$$V_{D1} = -\frac{V_S}{\left(1+3D+D^2\right)} \tag{34}$$

The current stress levels encountered by various diodes are detailed as follows:

$$I_{D1} = \frac{(2-D)I_0}{(1-D)*\left(1+3D+D^2\right)} \tag{35}$$

$$I_{D2} = \frac{I_0}{(1-D)*\left(1+3D+D^2\right)} \tag{36}$$

$$I_{D3} = \frac{I_0}{D*\left(1+3D+D^2\right)} \tag{37}$$

$$I_{D4} = \frac{I_0}{\left(1+3D+D^2\right)} \tag{38}$$

$$I_{D0} = \frac{I_0}{(1-D)} \tag{39}$$

The proposed Z-SQ-IBZ converter timing waveform is depicted in figure.7

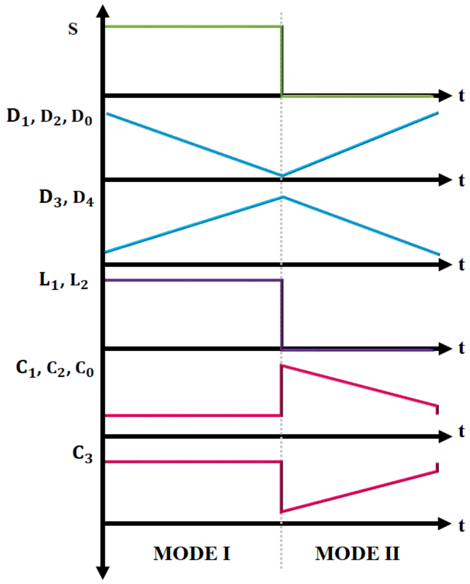

Fig. 7. Timing Diagram

Voltage is boosted thus, Z-SQ-IBZ converter effectively boosts the PV system output voltage. However, to capture improved energy from a PV system under varying environmental circumstances, MPPT are crucial components. It significantly optimizes power extraction from the solar panels.

3-3- Cray Fish Optimized RBFNN MPPT

3-3-1 RBFNN-based MPPT

The solar energy extracted from the PV system heavily relies on the dynamic environment. The power attained is influenced by solar irradiation and intensity. The maximum power extraction is crucial. It is suggested to use an RBFNN-based MPPT controller for maximizing power extracted from solar panels. RBF neural network is employed to implement an MPPT control technique, as it provides a nonlinear model with enhanced learning speed.

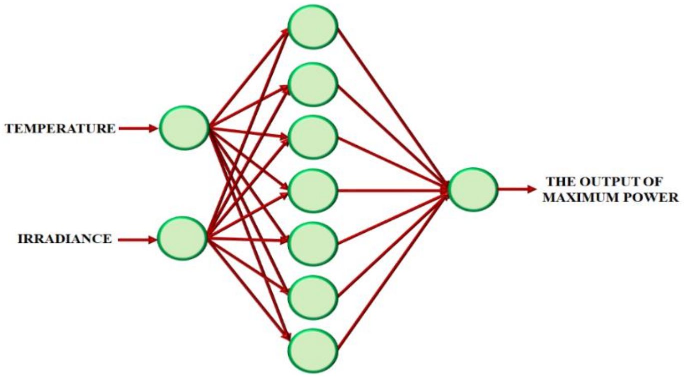

Fig. 8. RBFNN-based MPPT configuration

In RBFNN, the input of i^{th} hidden neuron is computed as follows:

$$k_i^q = \sqrt{\sum_j \left(w1_{i,j} - X_j^q\right)^2 .b1_i} \tag{40}$$

From eqn (39), j represents input neurons, while hidden layer neurons are represented as i, q^{th} input vector by q. Matrix represents the spatial relationship between the weight of hidden layer and input vector within a computational framework by measuring their distance.

$$w1_i - X^q \tag{41}$$

Bias vector, denoted as $b1$, is applied. Each neuron in hidden layer operates with base transfer function that is typically represented using a Gaussian function. This function's output is inversely proportional to distance from center of neuron. Gaussian function has following mathematical definition:

$$r(x) = \exp\left(-\frac{(x-a)^2}{b^2}\right) \tag{42}$$

Output of i^{th} hidden layer is calculated by,

$$r_i^q = \exp\left(-\left(k_i^q\right)^2\right) = \exp\left(-\left(w1_i - x^q .b1_i\right)^2\right) \tag{43}$$

A neural network is trained using a variety of datasets and environmental conditions until error is minimized. As illustrated in Figure 8, RBFNN is employed for MPPT control. Though, fine-tuning is necessary to achieve maximum photovoltaic power output. To this end, proposed RBFNN-based MPPT technique is enhanced using a bio-inspired algorithm. Specifically, RBFNN is optimized with the implementation of crayfish optimized algorithm, ensuring peak tracking power.

3-3-2 Cray Fish Optimization Algorithm

Crayfish behaviours, including as foraging, summer vacation, and competition, trigger the swarm intelligence optimization known as COA. These behaviours are divided into stages: foraging and competition stages focus on exploitation, while summer resort stage emphasizes exploration. Crayfish regulate their food consumption, which is regulated by temperature and follows positive distribution pattern.

Source of Inspiration:

First, the method defines a colony of crayfish, X, where the position of each crayfish signifies a possible solution $\left(X_i = \left\{X_{i,1}, X_{i,2}, X_{i,3}, .., X_{i,dim}\right\}\right)$.Characteristic quantity of optimization problem is dim. Fitness value of each solution X_i is determined by function $f(\cdot)$. Temperature, a random constant, regulates algorithm's exploration and exploitation. High temperatures lead to summer resort or competition stages, where crayfish either seek caves or compete for them. At appropriate temperatures, the foraging stage begins, where crayfish aim to find and consume food, representing the optimal solution. Each crayfish solution indicates a distinct combination of RBFNN parameters, including centres, spreads, and weights.

Food size and intake are influenced by fitness values $fitness_i$, and $fitness_{food}$, Crayfish adjust their positions accordingly. The alternating feeding behaviour is modelled using sine and cosine functions, with food intake following a positive distribution based on temperature. The integration of this optimization algorithm minimizes the power error.

Initialize Population:

Each crayfish is represented as a as $1 \times dim$ matrix in multi-dimensional optimization tasks, with each column denoting a possible solution. Variables $\left(X_{i,1}, X_{i,2}, X_{i,3}, .., X_{i,dim}\right)$ are constrained within specified upper and lower limits. In initialization phase of COA, collection of candidate solutions X is generated at random within solution space, which is determined by dimension dim and population size N. This initialization is mathematically characterised as follows:

$$X = \left[X_1, X_2, .., X_n\right] = \begin{bmatrix} X_{1,1} & \cdots & X_{1,j} & \cdots & X_{1,dim} \\ \vdots & \cdots & \vdots & \cdots & \vdots \\ X_{i,1} & \cdots & X_{i,j} & \cdots & X_{i,dim} \\ \vdots & \cdots & \vdots & \cdots & \vdots \\ X_{N,1} & \cdots & X_{N,j} & \cdots & X_{N,dim} \end{bmatrix} \quad (44)$$

10.22060/EEJ.2025.24346.5688

$X_{i,j}$ indicates position of i^{th} individual in j^{th} dimension, with its value determined by,

$$X_{ij} = lb_j + \left(ub_j - lb_j\right) \times rand \tag{45}$$

Lower bound lb_j and upper bound ub_j define constraints for j^{th} dimension, while $rand$ represents random number. Using these parameters, a randomized set of RBFNN configurations is created, initiating a search across an extensive parameter space.

3-3-3 Crayfish food intake and define temperature:

Definition of temperature is mathematically expressed in Eq. (45),

$$temp = rand \times 15 + 20 \tag{46}$$

Mathematical representation of crayfish intake is provided in Eq. (46), offering a detailed framework for its analysis.

$$p = C_1 \times \left(\frac{1}{\sqrt{2 \times \pi \times \sigma}} \times \left(-\frac{\left(temp - \mu\right)^2}{2\sigma^2} \right) \right) \tag{47}$$

It determines extent to which parameters of RBFNN are modified during optimization. This influences precision and efficiency of parameter adjustments.

Exploration:

When temperature exceeds 30, it becomes extremely elevated. Under these conditions, crayfish elect to retreat into cave for their summer vacation. Cave, represented as X_{shade}, is given below:

$$X_{shade} = \left(X_G + X_L\right) / 2 \tag{48}$$

Optimal position within current population is shown by X_L, and optimal position achieved after multiple rounds is represented by X_G. When a random value $rand$ is less than 0.5, it signifies that no other crayfish are competing for cave, enabling to occupy it for a summer retreat. During this process, Eq. (48) is employed for crayfish to enter cave.

$$X_{i,j}^{t+1} = X_{i,j}^{t} + C_2 \times \text{rand} \times \left(X_{\text{shade}} - X_{i,j}^{t} \right) \tag{49}$$

Current iteration number in this case is represented by t, and iteration number for following generation is represented by t + 1. Parameter C_2 follows a declining curve, as mathematically expressed in Eq. (49).

$$C_2 = 2 - \left(t / T \right) \tag{50}$$

Maximum number of iterations is denoted by T (49). In summer, crayfish focus on moving closer to a cave, which symbolizes an optimal solution. During this phase, they actively approach cave, thereby drawing nearer to the optimal result. This process improves exploitation capability of COA, allowing it to converge more rapidly. Furthermore, RBFNN parameter is adjusted toward optimal regions, promoting exploration of diverse solutions while avoiding premature convergence.

Exploitation:

Competition stage:

Other crayfish are striving for the same cave when temperature rises above 30 degrees and random number $rand$ is larger than or equal to 0.5. It compete to claim a cave under these circumstances, using computations in Eq. (50) as a guide.

$$X_{i,j}^{t+1} = X_{i,j}^{t} - X_{z,j}^{t} + X_{\text{shade}} \tag{51}$$

Here, z represents an individual crayfish chosen at random, as shown in Eq. (51).

$$z = round\left(rand \times \left(N - 1 \right) \right) + 1 \tag{52}$$

Crayfish participate in competitive interactions during Competition stage, changing their location in relation to another crayfish's position X_z. This positional change increases scope of COA's search and enhances its capacity to more efficiently explore and find best answers.

Foraging stage:

Ideal temperature for crayfish to feed is below 30 degrees. Crayfish migrate in direction of a food source during this time. They locate food and measure its size. Crayfish replace using their second and third walking legs to ingest food, tearing it apart with their claws if it is too abundant. Position of food, signified by X_{food}, is expressed as follows:

$$\mathrm{X_{food}} = \mathrm{X_G} \tag{53}$$

Quantity of food, denoted as Q, is characterized by specific parameters or measurements that determine its suitability for consumption or processing within the given context.

$$\mathrm{Q} = \mathrm{C_3} \times \mathrm{rand} \times \left(\mathrm{fitness_i} / \mathrm{fitness_{food}}\right) \tag{54}$$

Where $fitness_i$ characterizes fitness value of i^{th} crayfish, $fitness_{food}$ indicates fitness value of food location, and C_3 food factor, which indicates greatest food, has a constant value of 3. Crayfish use largest food's size to gauge size of other foods. $Q > (C_3 + 1)/2$ specifies that food is too large. Here is an example of a mathematical equation:

$$X_{food} = exp\left(-\frac{1}{Q}\right) \times X_{food} \tag{55}$$

Food is sequentially grasped and moved to mouth by second and third paws when it has been broken up into smaller bits. A arrangement of sine and cosine functions is utilized for simulate this alternating movement. Following foraging equation results from direct relationship between crayfish consumption and amount of food they acquire:

$$\mathrm{X_{i,j}^{t+1}} = \mathrm{X_{i,j}^{t}} + \mathrm{X_{food}} \times \mathrm{p} \times \left(\cos\left(2 \times \pi \times \mathrm{rand}\right) - \sin\left(2 \times \pi \times \mathrm{rand}\right)\right) \tag{56}$$

Crayfish simply wish to move to food and consume in the open when $Q \le (C_3 + 1)/2$ following is equation:

$$X_{i,j}^{t+1} = \left(X_{i,j}^{t} - X_{food}\right) \times p + p \times rand \times X_{i,j}^{t} \tag{57}$$

Crayfish modify their eating tactics throughout foraging stage based on mass of their food, represented by Q, with X_{food} standing for the best possible answer. When crayfish can handle Q's size, they eagerly approach it. On the other hand, an excessively big Q indicates important discrepancy between present location and ideal solution. Under these circumstances, X_{food} moves closer towards food. Additionally, randomness in crayfish's consumption algorithm is used to enhance its efficiency. By optimizing this process, COA gravitates toward an optimal solution, improving its capacity for exploitation and ensuring robust convergence.

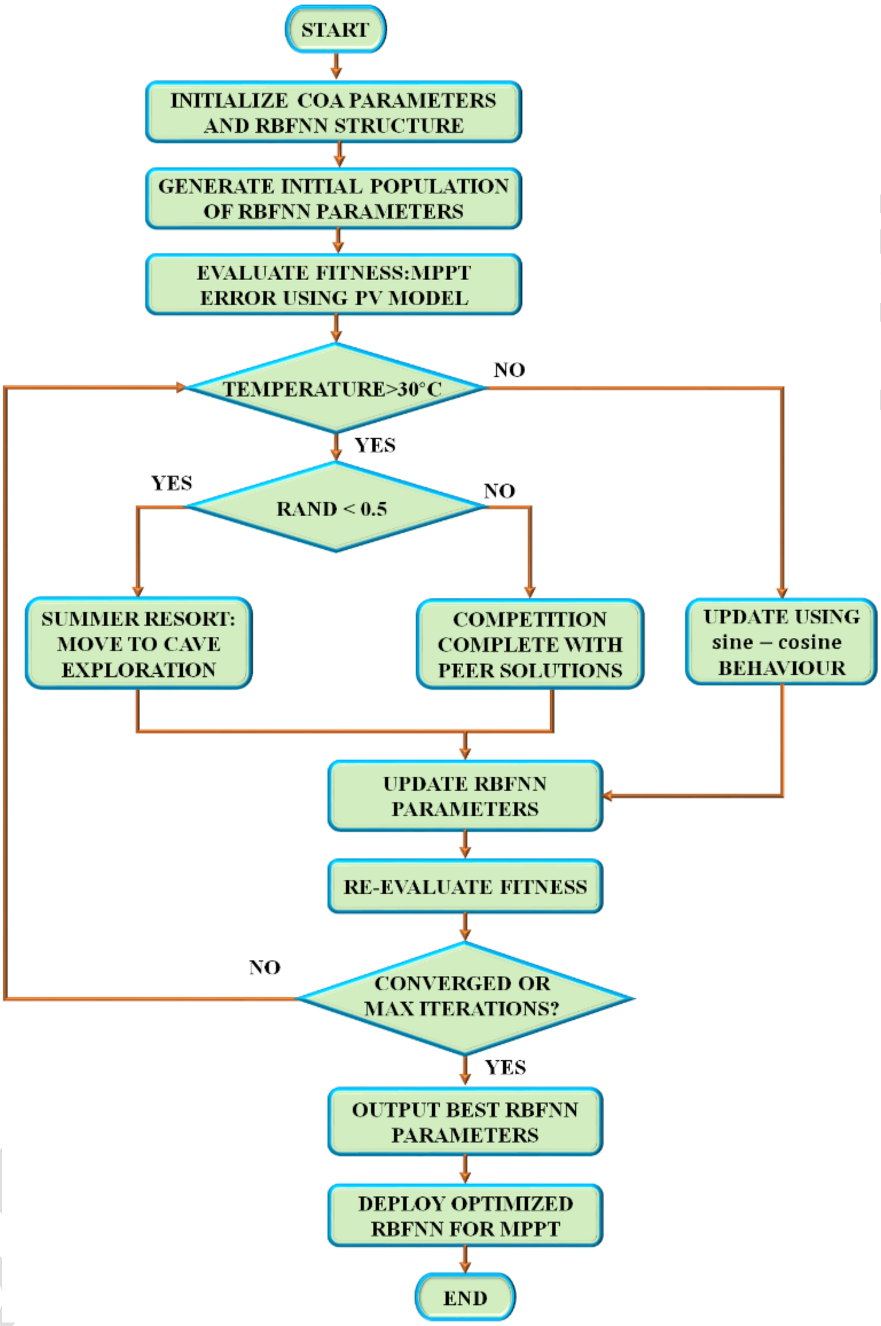

Fig. 9. Flowchart of COA based RBFNN MPPT

Figure.9 flowchart illustrates the COA. By iteratively adjusting weights and biases of RBFNN, this technique lowers prediction errors and improves accuracy factors like temperature and sun irradiance. Precision of network's predictions is greatly impacted by weights and biases in RBFNN, hence relationship between prediction errors and these parameters is crucial. Difference between network's output and actual target value is known as estimation error. To reduce this inaccuracy, weights and biases are changed throughout training. Utilizing both its exploration and exploitation capabilities, algorithm improves adaptability and learning efficiency of RBFNN using existing data. Synergy ultimately boosts performance and efficiency of PV system through accurate parameter estimation, enabling the attainment of maximum PV power with proposed crayfish-optimized RBFNN MPPT approach.

3-4 Bidirectional Converter

Depending on requirements of application, the bidirectional converter allows current to flow in both directions, facilitating effective power transmission between sources and loads. In EV powertrain applications, the BC manages voltage requirements by utilizing an additional battery to provide peak current during start-up and stepping up voltage when extra power is needed. The bidirectional DC-DC converter implemented in this research is depicted in figure.10

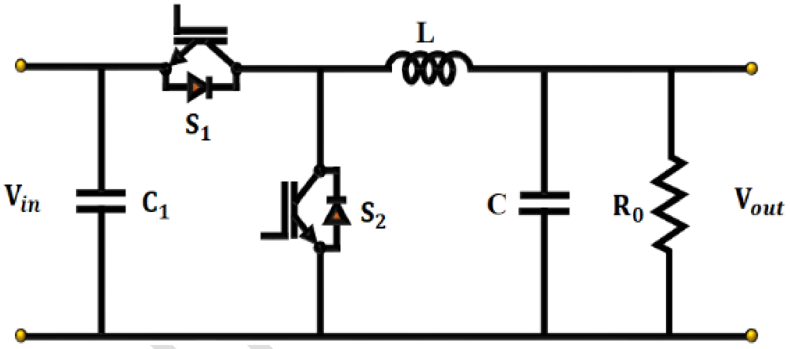

Fig. 10. Bidirectional Converter

The following describes the operation and design of converter: V_{in} stands for input voltage, and V_{out} for output voltage. BC functions in two modes: Boost mode (backward operation), which is controlled by switch S_2, and Buck mode (forward operation), which is controlled by switch S_1.

Step-down operation:

In this mode of operation, switch S_1 is turned on while S_2 is off, and output voltage is lower than input voltage. When charging a battery via DC grid, input current rises, flowing through S_1 and inductor L during

10.22060/EEJ.2025.24346.5688

S_1's activation. As S_1 turns off, inductor current decreases until next cycle, with battery being charged using the energy stored in the inductor.

Step-up operation:

Output voltage is greater than input voltage in this mode. With switch S_2 turned on and S_1 off, battery powers load. When S_2 is on, the inductor (L) and switch S_2 experience an increase in input current. As S_2 turns off, inductor current decreases until next cycle, allowing stored energy in L to flow through load.

Bidirectional DC-DC converter proposed in this research enables efficient battery charging and discharging, storing excess energy during high solar irradiance and supplying power when required. Z-SQ-IBZ converter effectively boosts PV system voltage for inverter and battery charging, while the Crayfish Optimized RBFNN MPPT ensures maximum power extraction. The proposed approach efficiently charges EV using PV system while ensuring adaptability to varying grid conditions, providing a scalable and energy-efficient solution.

4. Result and Discussion

Proposed Z-SQ-IBZ converter and crayfish optimized MPPT algorithm is implemented in MATLAB/Simulink environment. Comparison is made with conventional approaches which shows the efficiency of presented work. Table.2 denotes parameter specifications of developed work.

Table 2: *Specifications of the parameter*

Parameter	Specifications
PV System	
Open circuit voltage	37.25V
Short circuit current	8.95A
Rated Power	5kW
No. of panels connected in series	4
No. of panels connected in parallel	5
Z-SQ-IBZ converter	
Switching Frequency	10kHz
Main switch (S)	IGBT-FH40T65SPD (Si-Trench Field-Stop IGBT)
Diode D_1 and D_2	Fast recovery diode-MUR1560
Diode D_3 and D_4	Schottky-STPS20H100
Inductor L_1 and L_2	4.7mH
(C_1, C_2, C_3)	22μF
C_0	2200μF
Gate driver IC	IIR2110
DC-link capacitor	EPCOS B43504

Case 1: Constant Temperature & Constant Intensity

Figure.11 presents waveform of solar panel under constant temperature and constant intensity conditions. Figure.11 (a) shows PV panel waveform of temperature. It is maintained at a constant temperature of $35^0 C$. Figure.11 (b) shows the intensity waveform of solar panel. Intensity is stable at $1000W / sq.m$ throughout the system. Figure.11 (c) shows voltage waveform of PV panel. Constant voltage of $110V$ is attained by PV system. Figure.11 (d) shows current waveform of PV system. Initially, input current of Z-SQ-IBC gets varied and stabilized at $54A$ after $0.1s$. The PV panel voltage and current quickly reaches steady-state, maintaining stable operation under fixed condition.

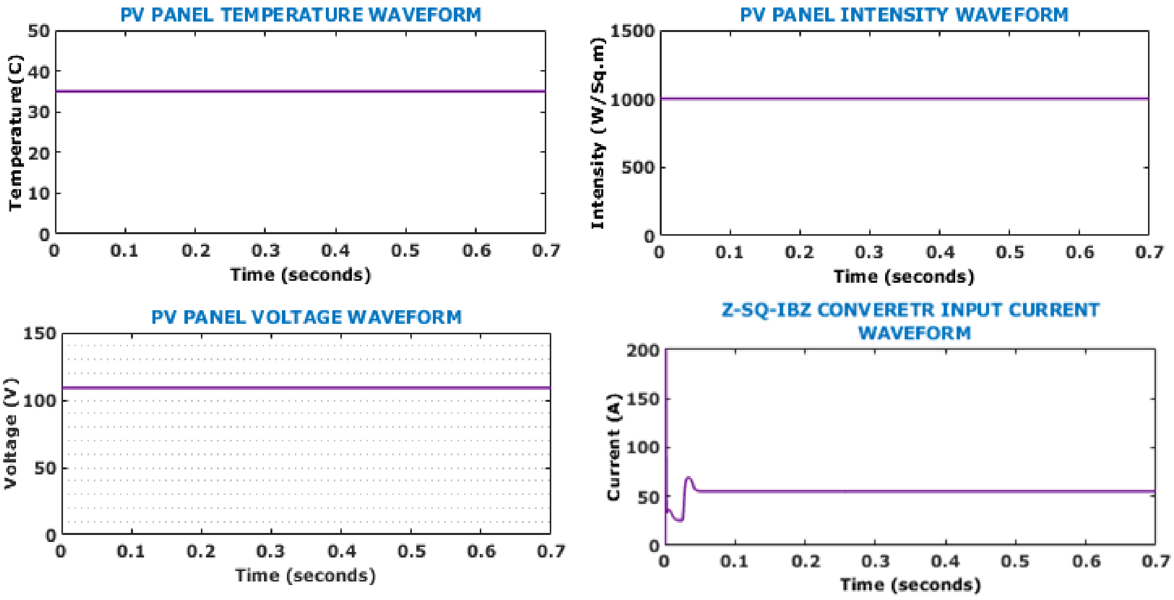

Fig. 11. PV panel waveform

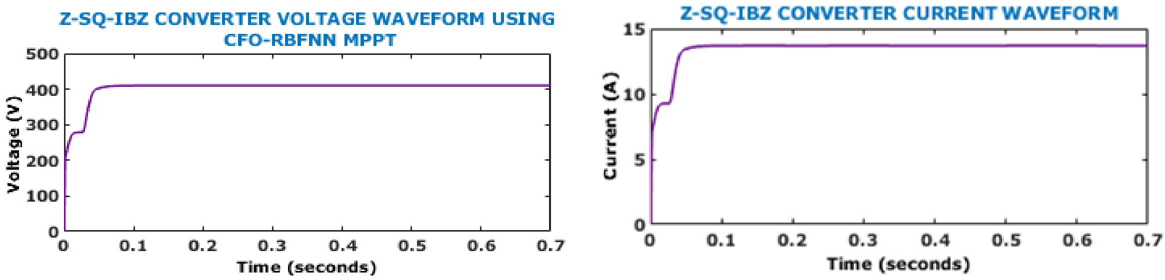

Fig. 12. Z-SQ-IB converter waveform

Figure.12 represents the proposed Z-SQ-IB converter with COA-RBFNN MPPT waveform under constant temperature and intensity conditions. Figure.12 (a) shows voltage waveform of converter. At initial phase, output voltage of converter is varied and soothed at $410V$. Figure.12 (b) shows output current of Z-SQ-IB converter is maintained at $14A$ with few initial fluctuations. Converter output voltage and current waveform indicate fast transient response with stable converter operations.

Case 2: Constant Temperature & Varying Intensity

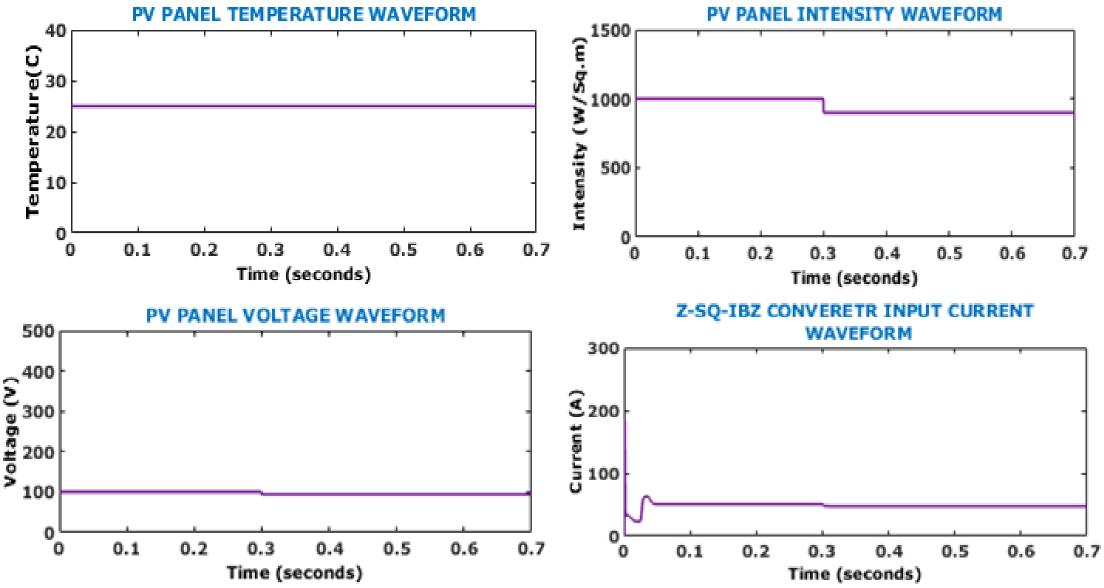

Fig. 13. PV panel waveforms

Figure.13 displays PV array waveform under persistent temperature and varying intensity condition. Figure.13 (a) displays temperature waveform of PV panel. Temperature is maintained at a constant value of 35^0C entire system. Figure.13 (b) shows the intensity waveform of PV system. Intensity of $1000W / sq.m.$ is preserved till $0.3s$ after that intensity value gets decreased to $900W / sq.m.$ Figure.13 (c) shows voltage waveform of solar panel. Input voltage of $98V$ is attained with minimal fluctuations. Figure.13 (d) shows the PV system waveform of current $50A$ is obtained with initial fluctuations.

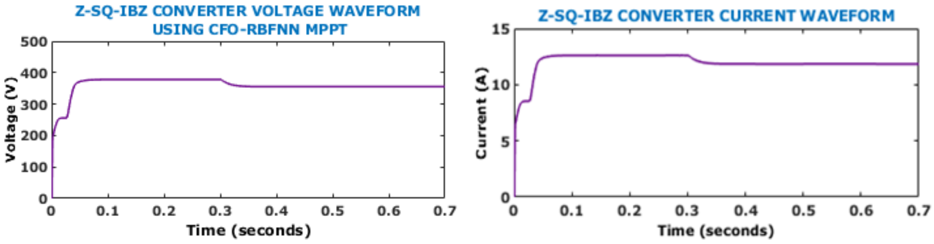

Fig. 14. Voltage and current waveform of converter

Figure.14 visualize proposed converter waveform in constant temperature and varying intensity circumstances. Figure.14 (a) indicates output voltage waveform of Z-SQ-IB converter. Through few initial fluctuations, the converter produces a constant output voltage of $340V$. Figure.14 (b) shows the Z-SQ-IB converter output current waveform. After $0.3s$, the converter produces a stable current of $12A$ is attained.

Case 3: Varying Temperature & Varying Intensity

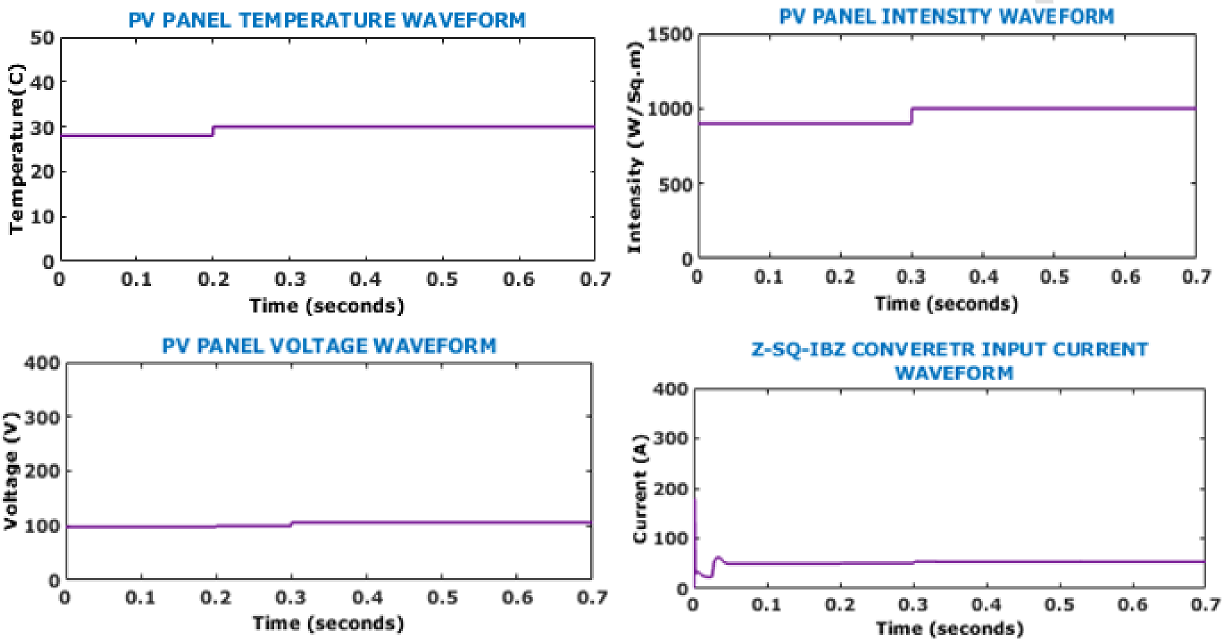

Fig. 15. PV panel waveform

Figure.15 illustrates the PV panel waveform under varying temperature and varying intensity conditions. Figure. 15 (a) shows temperature waveform of solar panel. Temperature gets elevated at 30^0C around $0.2s$. Figure.15 (b) shows the PV system intensity waveform. After $0.3s$, the intensity is increased from $900W/sq.m.$ to $1000W/sq.m.$ Figure.15 (c) shows voltage waveform of PV panel. Constant voltage of $110V$ is attained after initial fluctuations. Figure.15 (d) shows the current waveform, it attains $50A$ with little variations at the initial phase.

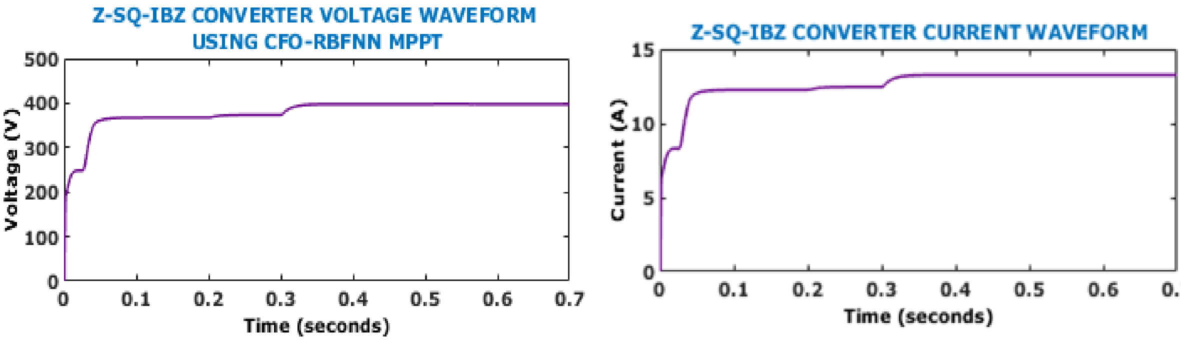

Fig. 16. Converter waveforms

Figure.16 determines voltage and current waveform of the proposed Z-SQ-IB converter under varying temperature and intensity conditions. Figure.16 (a) displays voltage waveform of converter. Z-SQ-IB converter produces an enhanced voltage of $400V$. Figure.16 (b) shows the converter current waveform. The current quickly rises from to $12A$ within $0.1s$, stabilizes thereafter, and experiences slight increments around 0.2 and 0.35 seconds, ultimately reaching nearly $14A$.

Grid Performance under 1000W

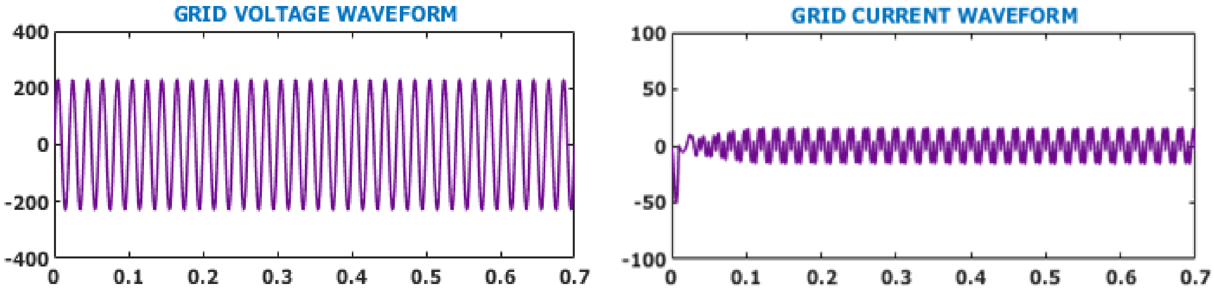

Fig. 17. Grid waveforms

Figure.17 reveals the current and voltage waveform of grid under $1000W$. Figure.17 (a) shows voltage waveform of grid. A stable voltage of $\pm 200V$ is produced, sinusoidal pattern indicating a stable voltage supply. Figure.17 (b) shows the grid current waveform. With few initial fluctuations, the current stabilizes at $\pm 15A$, ensuring steady current flow.

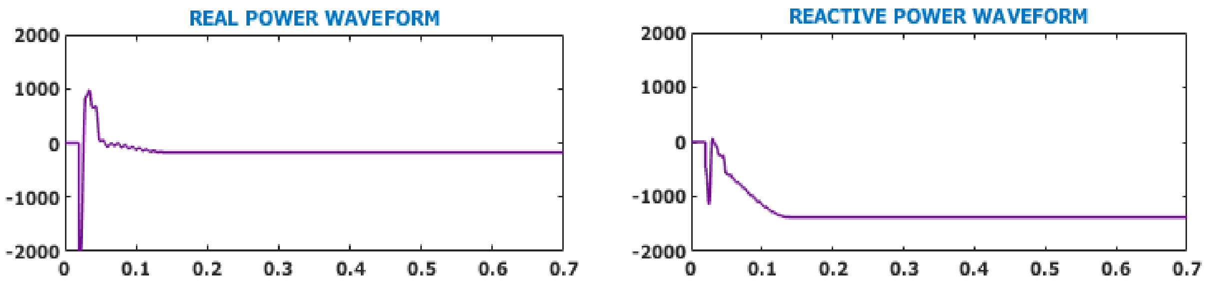

Fig. 18. Power waveform

Figure.18 exhibits the real and reactive power waveforms. Figure.18 (a) shows the waveform of real power. At initial phase, the real power spikes and then it gets stabilized with minor fluctuations. Figure.18 (b) shows the reactive power waveform. After a sudden drop, the reactive power is maintained at constant. The ability to maintain a nearly constant voltage under such dynamic conditions demonstrates the robustness of the proposed system and its suitability for field applications where weather changes unpredictably.

Grid Performance under 1500W

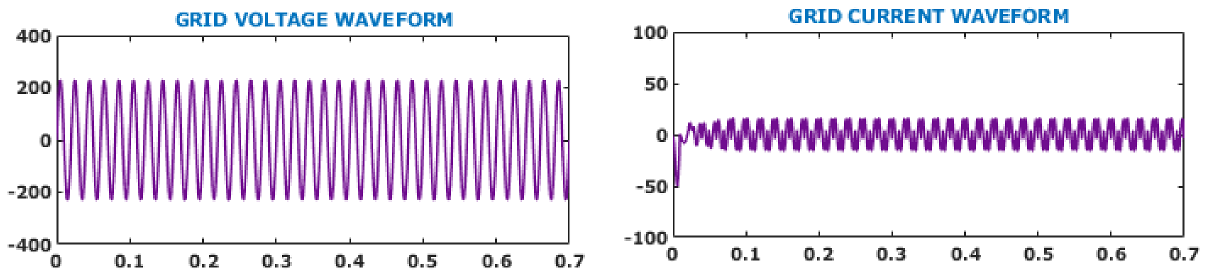

Fig. 19. Grid waveforms

Figure.19 demonstrates current and voltage waveform of grid under $1500W$ condition. Figure.19 (a) shows voltage waveform of the grid. A consistent voltage of $\pm 200V$ is obtained. Figure.19 (b) shows the grid current waveform. With the initial transient response, the current stabilized over $\pm 12A$. Grid voltage and current waveforms are sinusoidal, assuring grid synchronization and power quality.

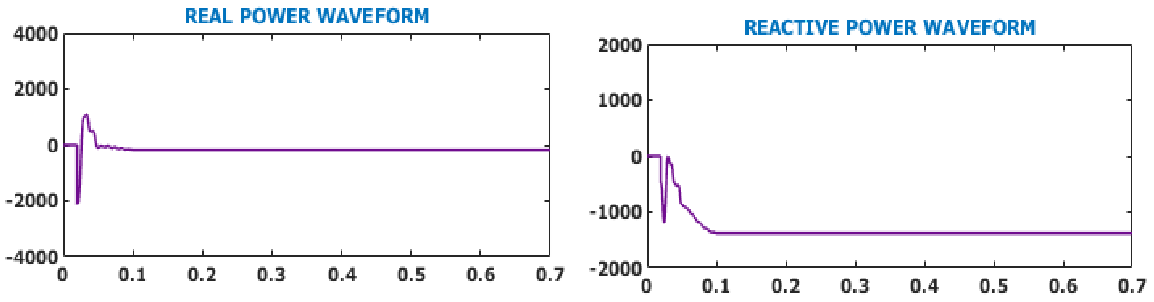

Fig. 20. Power waveform

Figure.20 presents real and reactive power waveforms. Initially, real power exhibits a sharp negative spike, followed by a rapid positive surge, after these fluctuations within $0.1s$, it stabilizes for the remaining duration. The reactive power drops after $0.1s$ it stabilizes throughout the system.

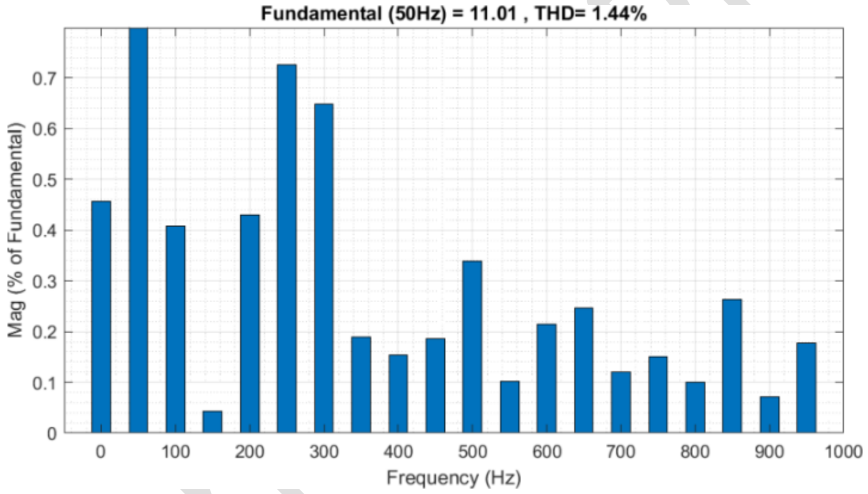

Fig. 21. THD waveform

Figure.21 represents the THD waveform. It shows the distribution of harmonics, presenting the highest amplitude at fundamental frequency of $50\,Hz$. A THD value of 1.44% distortions, indicates relatively low harmonic distortion, reflecting good quality. This ensures efficient and dependable operation for the EV charging station and its grid connections. The distortions >5%, complying the IEEE standards and ensuring power quality improvement.

Table 3. Comparison of efficiency

Converters	Accuracy
Zeta [25]	88.5%
Boost [26]	92.43%
Quadratic Boost [27]	94.60%

Non-Isolated Hybrid Zeta [28]	95.20%
Interleaved Dual Buck-Boost [29]	96%
Proposed	96.63%

Table 3 displays the proposed converter efficiency with conventional converters. It shows a steady rise in efficiency across various converters, from 88.50% with the Zeta converter [25] to 96.63% with the proposed converter. This graph highlights advancements introduced by the Z-SQ-IBZ converter's superior efficiency, positioning it as ideal for minimizing energy losses and boosting performance in renewable energy-powered EV charging systems.

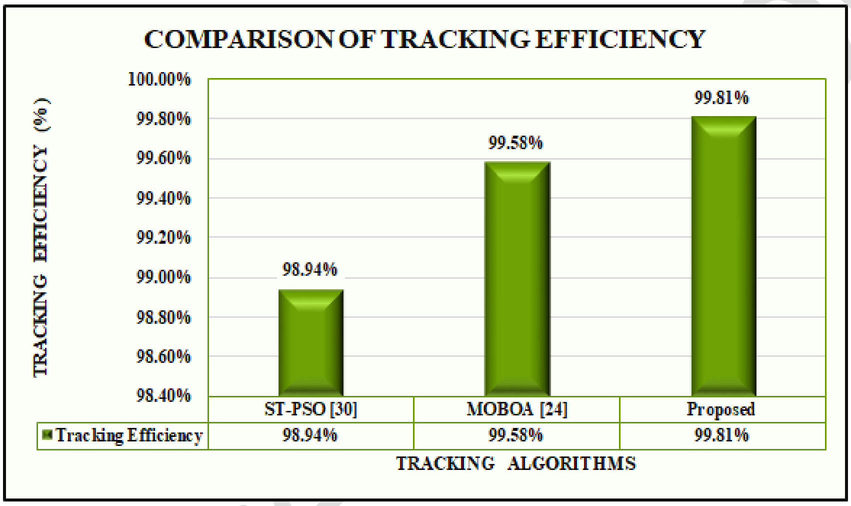

Fig. 22. Comparison of tracking efficiency.

Figure.22 visualizes a comparative analysis of MPPT algorithms' tracking efficiency. The table compares various MPPT algorithms in a renewable energy-fed EV charging system. It highlights the proposed algorithm's higher tracking efficiency of 99.81%, surpassing Self-Tuning (ST)-PSO [30] (98.94%), and Multi-Objective Bayesian Optimization Algorithm (MOBOA) [24] (99.58%). This efficiency demonstrates the proposed COA algorithm's ability to optimize energy extraction under changing conditions, emphasizing its potential for enhancing EV charging systems and advancing sustainable transportation.

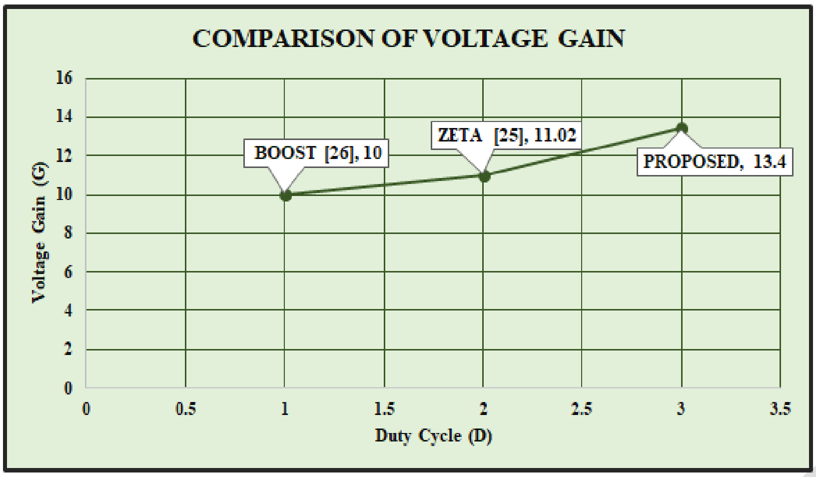

Fig. 23. Comparison of voltage gain

Figure.23 displays the voltage gain comparison for renewable energy-fed EV charging converters, showcasing that proposed converter achieves highest voltage gain (13.4), outperforming conventional boost (10) and zeta (11.02) converters. This superior voltage gain enhances performance by ensuring stable and elevated voltage levels, making the proposed converter ideal for efficient battery charging in EV systems, while supporting renewable energy integration.

Table 4. Converter loss breakdown

$$\boldsymbol{P_{loss} = P_{sw} + P_{cond,IGBT} + P_{diode} + P_{L,Cu} + P_{L,core} + P_{C,\,ESR} + P_{drv/misc}}$$

Loss Item	Equation	Value
IGBT Switching loss P_{sw}	$P_{sw} = \left(E_{on} + E_{off}\right) f_s$	$40W$
IGBT Conduction $P_{cond,IGBT}$	$P = V_{CE(sat)} I_{avg,on}$	49W
Diodes (fast recovery + Schottky) P_{diode}	$P = V_f I_{avg}$	26.8W
Inductor copper $P_{L,Cu}$	$P = I_{rms}^2 R_{DC}$	50W
Inductor core $P_{L,core}$	$P = kf^{\alpha} B^{\beta} V_c$	12W
Capacitor ESR, $P_{C,ESR}$	$P = I_{rms}^2 I_{ESR}$	4W
Gate drive and control $P_{drv/misc}$	Total sum	3W
Snubber/stray	estimated	15W
Total		=200W

Table 4 presents the detailed power loss analysis of the proposed Z-SQ-IBZ converter and identifies the contributions of the individual components to the total system loss. The total power loss is calculated as the summation of the switching loss, IGBT conduction loss, diode loss, inductor copper and core losses and, capacitor ESR loss, gate drive and miscellaneous control losses, and estimated snubber/stray losses. The IGBT switching and conduction losses are 40 W and 49 W, respectively. Diode losses alone account for 26.8 W, which comprises fast recovery and Schottky diodes. Inductor copper loss dominates with 50 W, while the core loss is 12 W. Capacitor ESR loss contributes marginally at 4 W, as does gate drive loss, at 3 W, with snubber and stray losses estimated at 15 W. These accumulate to 200 W of cumulative loss and validate the thermal and efficiency profile of the converter under rated operating conditions.

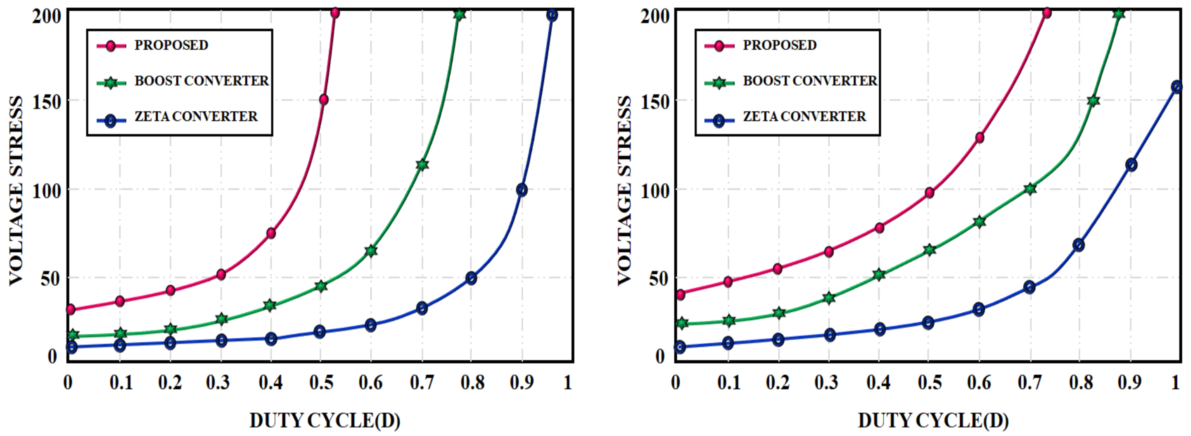

Fig. 24. Voltage stress across diode and switches

Figure.24 exhibits comparison of various converters voltage stress across diode and switches. Proposed topology showcases lowest voltage stress with improving component reliability, which increases gradually across the entire duty cycle range, ensuring minimal stress compared to the other converters. Boost converter [26] demonstrates moderate voltage stress that escalates more rapidly with duty cycles relative to the proposed converter. Zeta converter [25] exhibits the highest voltage stress, with a sharp rise as the duty cycle nears 0.5 and beyond. The proposed converter stands out for its lower voltage stress, contributing to reliability and longevity in renewable energy-fed EV charging stations.

5. Conclusion

This research introduces an advanced PV energy system that employs a Z-SQ-IBZ converter to elevate low voltage of PV system, ensuring optimal stabilization of output voltage. Maximum power is efficiently tracked using a COA-based RBFNN MPPT controller, which provides precise outputs with improved tracking performance. The surplus energy generated by solar panel is kept in battery and later delivered to grid during periods of high energy demand or when PV system unable to generate sufficient power for EV applications. Additionally, the single-phase VSI enables smooth operation, optimizing the inverter's overall capabilities economically. The system's performance is validated through MATLAB/Simulink simulations, showing Z-SQ-IBZ converter achieving a 96.63% efficiency and enhanced tracking efficiency of 99.81%, delivering consistent and maximum power with relatively low distortion via effective grid synchronization. In future work, a prototype will be built on a laboratory scale using a DSP or an FPGA-based digital control platform to experimentally validate converter performance, MPPT response, and grid synchronization overall under real-time operating conditions. This will enable a thorough evaluation of power quality, efficiency of the converter, and dynamic response, filling the gap between simulation and implementation.

Reference

[1] A.S. Abdulbaqi, "Innovative Control Strategies for Dynamic Load Management in Smart Grid Techniques Incorporating Renewable Energy Sources," KHWARIZMIA, pp. 73–83, 2023.

[2] C.U. Rao, A.S. Maheswara, B.V. Babu, B.M. Krishna, and P. Sudheer, "Performance Validation of PV Cell Configurations," Journal of Advanced Research in Dynamical and Control Systems, Vol. 11, no. 6, pp. 1943023X, 2019.

[3] Y. ALAIWI, T. Ahmed, "Solar Air Heaters Classifications and Enhancement: A Review," Babylonian Journal of Mechanical Engineering, Vol. 2024, pp. 71-80, 2024.

[4] K.S. Kavin, P. Subha Karuvelam, M. Devesh Raj, and M. Sivasubramanian, "A novel KSK converter with machine learning MPPT for PV applications," Electric Power Components and Systems, pp. 1-19, 2024.

[5] M.K. Senapati, O. Al Zaabi, K. Al Hosani, K. Al Jaafari, C. Pradhan, and U.R. Muduli, "Advancing electric vehicle charging ecosystems with intelligent control of DC microgrid stability," IEEE Transactions on Industry Applications 2024.

[6] R.K. Lenka, A.K. Panda, R. Patel, and J.M. Guerrero, "PV integrated multifunctional off-board EV charger with improved grid power quality," IEEE Transactions on Industry Applications, Vol. 58, No. 5, pp. 5520-5532, 2022.

[7] K. S. Kavin, P. Subha Karuvelam, "PV-based grid interactive PMBLDC electric vehicle with high gain interleaved DC-DC SEPIC Converter," IETE Journal of Research, Vol. 69, No. 7, pp. 4791-4805, 2023.

[8] Y. Li, S. Sahoo, T. Dragičević, Y. Zhang, and F. Blaabjerg, "Stability-oriented design of model predictive control for DC/DC boost converter." IEEE Transactions on Industrial Electronics, Vol. 71, No. 1, pp. 922-932, 2023.

[9] S.V. Naresh, S. Peddapati, and M.L. Alghaythi, "A novel high quadratic gain boost converter for fuel cell electric vehicle applications," IEEE Journal of Emerging and Selected Topics in Industrial Electronics, Vol. 4, No. 2, pp. 637-647, 2023.

[10] G. Zhang, Z. Wu, S.Y. Shenglong, H. Trinh, and Y. Zhang, "Four novel embedded Z-source DC–DC converters," IEEE Transactions on Power Electronics, 2021, vol. 37, no. 1, pp. 607-616.

[11] N. El-Zarif, C.J. Fayomi, M. Ali, M. Amer, A. Hassan, and Y. Savaria, "A Systematic Approach for PLL-Based Zeta Power Converter Control," IEEE Access 2024.

[12] V. Chapparya, A. Dey, and S.P. Singh, "A Novel Non-Isolated Boost-Zeta Interleaved DC-DC Converter for Low Voltage Bipolar DC Micro-Grid Application," IEEE Transactions on Industry Applications, Vol. 59, No. 5, pp. 6182-6192, 2023.

[13] A.V. Solanke, S.K. Verma, S. Kumar, B. Oyinna, and K.E. Okedu, "MPPT For Hybrid Energy System Using Machine Learning Techniques." Journal of Modern Technology, pp. 19-37, 2024.

[14] A.I. Ali, H.H. Mousa, H.R. Mohamed, S. Kamel, A.S. Hassan, Z.M. Alaas, E.E. Mohamed, and A.R. Abdallah, "An enhanced P& O MPPT algorithm with concise search area for grid-tied PV systems." IEEE Access, Vol. 11, pp. 79408-79421, 2023.

[15] A.K. Gupta, R.K. Pachauri, T. Maity, Y.K. Chauhan, O.P. Mahela, B. Khan, and P.K. Gupta, "Effect of various incremental conductance MPPT methods on the charging of battery load feed by solar panel." Ieee Access, Vol. 9, pp. 90977-90988, 2021.

[16] S.R. Kiran, C.H. Basha, V.P. Singh, C. Dhanamjayulu, B.R. Prusty, and B. Khan, "Reduced simulative performance analysis of variable step size ANN based MPPT techniques for partially shaded solar PV systems," IEEE access, 2022, Vol. 10, pp. 48875-48889.

[17] K. Ullah, M. Ishaq, F. Tchier, H. Ahmad, and Z. Ahmad, "Fuzzy-based maximum power point tracking (MPPT) control system for photovoltaic power generation system," Results in Engineering, Vol. 20, pp. 101466, 2023.

[18] K.H. Chao, M.N. Rizal, "A hybrid MPPT controller based on the genetic algorithm and ant colony optimization for photovoltaic systems under partially shaded conditions," Energies, Vol.14, No. 10, pp. 2902, 2021.

[19] I.S. Millah, P.C. Chang, D.F. Teshome, R.K. Subroto, K.L. Lian, and J.F. Lin, "An enhanced grey wolf optimization algorithm for photovoltaic maximum power point tracking control under partial shading conditions," IEEE Open Journal of the Industrial Electronics Society, Vol. 3, pp. 392-408, 2022.

[20] E.S. Wirateruna, A.F. Millenia, "Design of MPPT PV using particle swarm optimization algorithm under partial shading condition," International Journal of Artificial Intelligence & Robotics (IJAIR), Vol. 4, No. 1, pp. 24-30, 2022.

[21] H.B. Percin, A. Caliskan, "Whale optimization algorithm based MPPT control of a fuel cell system," International journal of hydrogen energy, Vol. 48, No. 60, pp. 23230-23241, 2023.

[22] K. Xia, Y. Li, B. Zhu, "Improved photovoltaic MPPT algorithm based on ant colony optimization and fuzzy logic under conditions of partial shading," IEEE Access 2024.

[23] T. Mariprasath, C.H. Basha, B. Khan, and A. Ali, "A novel on high voltage gain boost converter with cuckoo search optimization based MPPTController for solar PV system," Scientific reports, Vol. 14, No. 1, pp. 8545, 2024.

[24] S. Noroozi, H.Shayanfar, and M. Nasirian, "A Bayesian Multiobjective Approach Based on GMPPT for PV Arrays," International Transactions on Electrical Energy Systems, Vol. 2022, No. 1, pp. 3307679, 2022.

[25] K.A. Anson, F.H. KP, H.J. Jacob, and S. Mathew, "Zeta Converter with Improved Voltage Conversion Gain," International Journal of Engineering Research & Technology (IJERT), Vol. 10, No. 06, pp. 422-427, 2021.

[26] S. Sadaf, M.S. Bhaskar, M. Meraj, A. Iqbal, N. Al-Emadi, “Transformer-less boost converter with reduced voltage stress for high voltage step-up applications,” IEEE Transactions on Industrial Electronics, Vol. 69, No. 2, pp. 1498-1508, 2021.

[27] A.S. Jana, C.H. Lin, T.H. Kao, and C.H. Chang, “A high gain modified quadratic boost DC-DC converter with voltage stress half of output voltage,” Applied Sciences, Vol. 12, No. 10, pp. 4914, 2022.

[28] P.L. Santosh Kumar Reddy, Y.P. Obulesu, S. Singirikonda, M. Al Harthi, M.S. Alzaidi, and S.S. Ghoneim, “A non-isolated hybrid Zeta converter with a high voltage gain and reduced size of components,” Electronics, Vol. 11, No. 3, pp. 483, 2022.

[29] S. Krithiga, N. Sujitha, G.J. Sandeep, R. Gokulnath, and P.S. Subudhi, “FLC-based, PV-fed interleaved dual buck-boost converter for EV battery charging applications,” Heliyon, Vol. 8, No. 4, 2022.

[30] A. Refaat, A. Elbaz, A.E. Khalifa, M.M. Elsakka, A. Kalas, and M. H. Elfar, “Performance evaluation of a novel self-tuning particle swarm optimization algorithm-based maximum power point tracker for porton exchange membrane fuel cells under different operating conditions,” Energy Conversion and Management, Vol. 301, pp. 118014, 2024.